

Journal of Biomedical Optics

SPIEDigitalLibrary.org/jbo

Design of a handheld optical coherence microscopy endoscope

Vrushali R. Korde
Erica Liebmann
Jennifer K. Barton

Design of a handheld optical coherence microscopy endoscope

Vrushali R. Korde,^a Erica Liebmann,^b and Jennifer K. Barton^{a,c}

^aUniversity of Arizona, College of Optical Sciences, 1630 East University Boulevard, Tucson, Arizona 85721

^bUniversity of Arizona, Department of Material Science and Engineering, 1235 East James E. Rogers Way, Tucson, Arizona 85721

^cUniversity of Arizona, Department of Biomedical Engineering, 1657 East Helen Street, Tucson, Arizona 85721

Abstract. Optical coherence microscopy (OCM) combines coherence gating, high numerical aperture optics, and a fiber-core pinhole to provide high axial and lateral resolution with relatively large depth of imaging. We present a handheld rigid OCM endoscope designed for small animal surgical imaging, with a 6-mm diam tip, 1-mm scan width, and 1-mm imaging depth. *X-Y* scanning is performed distally with mirrors mounted to micro galvanometer scanners incorporated into the endoscope handle. The endoscope optical design consists of scanning doublets, an afocal Hopkins relay lens system, a 0.4 numerical aperture water immersion objective, and a cover glass. This endoscope can resolve laterally a 1.4- μm line pair feature and has an axial resolution (full width half maximum) of 5.4 μm . Images taken with this endoscope of fresh *ex-vivo* mouse ovaries show structural features, such as *corpus luteum*, primary follicles, growing follicles, and fallopian tubes. This rigid handheld OCM endoscope can be useful for a variety of minimally invasive and surgical imaging applications. © 2011 Society of Photo-Optical Instrumentation Engineers (SPIE). [DOI: 10.1117/1.3594149]

Keywords: endoscopy; minimally invasive imaging; ovaries; optical coherence imaging.

Paper 10523RR received Sep. 24, 2010; revised manuscript received Apr. 29, 2011; accepted for publication May 4, 2011; published online Jun. 29, 2011.

1 Introduction

Optical coherence tomography (OCT) is a high-resolution cross-sectional imaging technique that uses light backscattered from tissue index of refraction mismatches to create an image.¹ OCT is analogous to ultrasound, where the image is created using backscattered sound waves. However, unlike ultrasound, a Michelson interferometer is needed to measure the backscattered light waves due to the faster speed of light and detector temporal integration times. This method of time-gating photons allows OCT to detect depth-resolved structural information in highly scattering tissue up to 2 mm in depth. Conventional OCT systems use low numerical aperture (NA) optics in the sample arm to achieve a 2-mm depth of focus, which results in lateral resolutions from 10 to 40 μm . To achieve higher and more uniform lateral resolution without image processing, a higher numerical aperture objective can be used along with dynamic focus tracking throughout the penetration depth.² Alternatively, image-processing techniques, such as deconvolution^{3,4} and inverse scattering,⁵ can be used to improve lateral resolution. Additionally, recently a Gabor-based fusion technique demonstrated 2- μm lateral resolution.^{6,7} Each of these techniques requires increased hardware and/or software complexity to achieve uniform lateral resolution over a large depth range.

An alternative method for achieving high lateral resolution images is to use a high numerical aperture objective in the sample arm and scan laterally in two dimensions to create an *en face* image. Confocal microscopy is a well-established imaging modality that operates in this manner. In confocal

microscopy, a focal volume in the sample is imaged back to a pinhole, which aids in rejecting out-of-focus backscattered light. Even with the use of pinhole imaging, confocal microscopy is limited to a penetration depth of a couple hundred microns in highly scattering samples such as tissue. An optical coherence microscope (OCM) is a combination of an OCT system and a confocal microscope. Like OCT, it utilizes time gating to increase the rejection of out-of-focus backscattered light. Like confocal microscopy, it contains high numerical aperture optics coupled to a fiber pinhole to provide high lateral resolution. The result is a system that can have ultrahigh lateral resolution and a penetration depth of several hundred microns.

We have previously described a tabletop OCM system (Fig. 1).⁸ Briefly, the system contains a superluminescent diode source centered at 835 nm with an 80-nm full width half maximum (FWHM) bandwidth, providing a theoretical axial resolution of 3.8 μm . The light intensity is split by a 50:50 single-mode fiber coupler into a reference arm and sample arm. In the sample arm; light from the fiber is collimated and reflected off two *X* and *Y* scanning galvanometer mounted mirrors that perform *en face* scanning synchronized with data sampling. A 20X infinity-corrected water-immersion microscope objective produces a 4- μm lateral resolution with a 1-mm \times 1-mm field of view. In the reference arm, fiber polarization adjustment paddles (not shown) match polarization states in the sample and reference arms to maximize fringe visibility. Given that the source spectrum is large and close to the visible range, dispersion compensation for the sample arm objective is necessary and provided by a BK7 prism pair. The light is focused onto a small lightweight mirror glued on a piezoelectric stack. To achieve modulation,

Address all correspondence to: Vrushali R. Korde, University of Arizona, College of Optical Sciences, 1630 East University Boulevard, Tucson, Arizona 85721. Tel: 310-650-7460; E-mail: Vrushali.R.Korde@gmail.com.

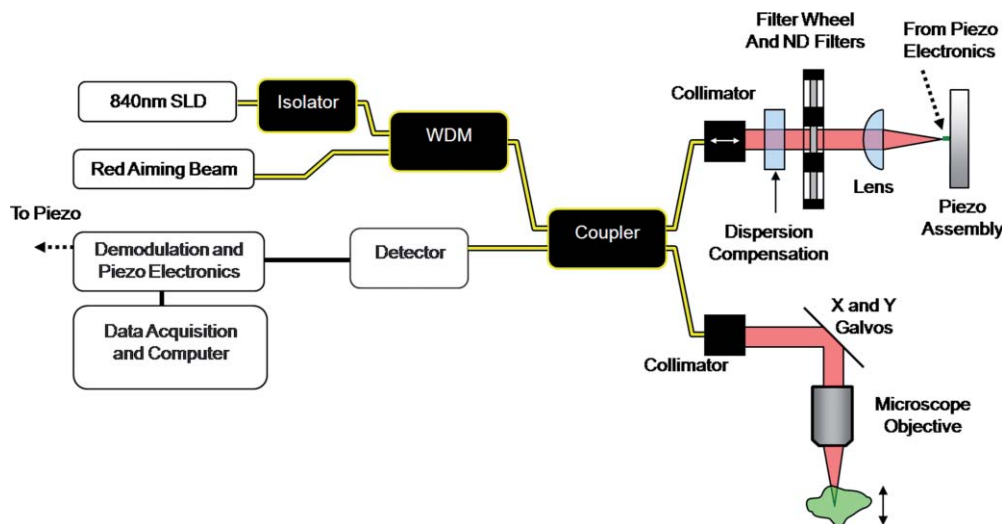


Fig. 1 Block diagram of the OCM system (WDM = wavelength division multiplexer).

the piezoelectric stack is driven by a sinusoidal signal at its resonance frequency, 120 kHz, to a displacement of $352 \text{ nm} = 0.42\lambda$.⁹ At this oscillation magnitude, the sum of the first two harmonic powers of the coherence fringe signal is insensitive to the interferometer phase drift. A photodetector with integrated amplifier and high-pass filter senses the signal from the sample and reference arms and eliminates the large direct-current component. The interferometric signal is then demodulated, and the signal components are acquired by a data acquisition board at a rate of up to 6×10^4 pixels/s. After signal combination and logarithmic compression the computer displays the *en face* image.

A tabletop system is appropriate for imaging *ex vivo* samples, nonbiological samples, and readily accessible tissues, such as forearm skin *in vivo*. However, for surgical or minimally invasive imaging, an endoscope is needed. In particular, we desired the ability to image tissue microstructure and cell nuclei of the ovaries of mice *in vivo*. Our Institutional Animal Care and Use Committee–approved protocol allows repeat, surgical access to the ovary to monitor the progression of ovarian cancer. To provide adequate imaging with a minimum of trauma, it was determined that a rigid, forward-looking endoscope was necessary, with a length of at least 30 mm in order to reach the organ of interest and to be able to clearly view the surgical field. The maximum allowable outer diameter of the endoscope was 6 mm to fit through the surgical incision. The probe also needed a relatively large 1-mm field of view to visualize a large percentage of the target tissue. To visualize cell nuclei the lateral spot (Airy disk) radius requirement was no larger than $1.5 \mu\text{m}$. The axial (out-of-plane) resolution needed to be less than a cell diameter, or $\sim 10 \mu\text{m}$. Ovary tissue is extremely highly scattering ($\mu_s \sim 161 \text{ cm}^{-1}$).¹⁰ To enable detection of weak reflections from $500 \mu\text{m}$ deep, a very high dynamic range of 70 dB was necessary. Because surgical placement of the probe could be difficult and the probe might not be in direct contact with the ovary, a total depth adjustment (imaging range) of 1 mm was needed. Finally, based on experience imaging the ovaries of women *in vivo*, images had to take <4 s to acquire to minimize motion artifacts, preferably faster. These specifications are summarized in Table 1.

A literature survey was conducted to determine if an appropriate endoscope design already existed or to discover potential design elements that could be utilized. Most endoscopes that have been developed for OCT are side firing. These probes are ideal for imaging tubular organs, such as the colon, esophagus, and trachea. The first OCT endoscope developed in 1996 had a lateral resolution of $40 \mu\text{m}$.^{11,12} In this side-firing endoscope design, still commonly used today, the light from the distal end of the fiber is focused by a gradient-index (GRIN) lens and reflected perpendicular to the probe axis with a microprism. 3-D imaging using this design is possible by using a spiral scanning fiber endoscope probe¹³ or incorporating a 2-D scanning unit, such as a two-axis microelectromechanical system (MEMS).¹⁴

A forward-firing probe is preferred in certain imaging situations because it is easier to position the probe over the target tissue. The optical design and scanning mechanisms of a forward-firing endoscope are more technically challenging, and the forward-imaging probes reported thus far for OCT are relatively large, ranging from 1.65 to 7.5 mm.¹⁵ The first forward-imaging endoscope was designed in 1997 by Sergeev et al.¹⁶; it used an electromechanical unit to move a fiber tip across the imaging plane of a stationary lens system. This system achieved a 2.2-mm-diam flexible OCT probe. This design is still used in current research,^{17,18} and there have been modifications to the mechanism of fiber scanning, including using electroactive polymers,¹⁹ piezoactuators,^{20,21} thermoelectric actuators,²² magnetic actuators,²³ and resonant scanning.^{24,25} Other methods of forward scanning include counter-rotating GRIN lenses,^{26,27} which have the smallest diameter at 1.65 mm, and MEMS 1-D^{22,28–30} and 2-D scanning.³¹ All these designs used relatively low NA sample arm optics.

A straightforward scanning approach uses galvanometer-mounted mirror scanning at the proximal end of a rigid OCT endoscope containing high NA optics. This method of scanning has been reported with axial and lateral resolutions of $8\text{--}20 \mu\text{m}$.^{32,33} This method of scanning is also used in the only other OCM endoscope developed to date, to the authors' knowledge.³⁴ This endoscopic system has a 0.8 NA, $<2\text{-}\mu\text{m}$ measured spot radius, $<4\text{-}\mu\text{m}$ axial resolution, and an imaging speed of four images per second. This endoscope has an 8-mm

Table 1 Optical properties and physical requirements of the OCM endoscope.

Specification	Value	Driving Factor
Lateral resolution (Airy disk radius)	1.5 μm	Ability to visualize cell nuclei
Axial resolution	10 μm	Size of a cell
Full field of view in tissue	1 mm	Size of mouse ovary
Imaging depth range	1 mm	Placement in abdomen
Dynamic range	70 dB	Optical properties of ovary
Packaged diameter	6 mm	Size of surgical incision
Packaged length	>30 mm	Depth to ovary in mouse, clear visualization of imaging field
Image acquisition speed	<4 s/image	Ability to hold still during surgery
NA in fiber space	0.14	Single mode fiber
NA in tissue space	0.4	Derived
n in tissue space	1.34	Assumed similar to water
Magnification, tissue to fiber	2.9	Derived
Focus compensator	Outer housing	Operational simplicity

o.d. and a $242 \times 260\text{-}\mu\text{m}$ field of view, and has successfully imaged human colon *ex vivo* and human skin *in vivo* with cellular resolution.

Our application required a unique OCM endoscope design that combined high lateral resolution (<1.5-mm Airy disk radius), moderate diameter (6 mm), and large field of view (1 mm). The initial design for our endoscope has been previously presented.³⁵ Here, we present a fully realized and tested OCM endoscope design to meet these requirements, which replaces the sample arm of our previously developed table top OCM system.

2 Materials and Methods

The specifications of Table 1 were used to determine the optical design of the endoscope. The packaged diameter of 6 mm allowed for an optical clear aperture of 3.6 mm. Using smaller diameter optics, in general, will reduce the NA of the optical system, which reduces the diffraction-limited lateral resolution. This can be seen from the following equations, where f is the focal length and λ_0 is the center wavelength of the light source (835 nm in our case):

$$\text{NA} \approx \frac{\text{Entrance Pupil Diameter}}{2f},$$

$$\text{Lateral Spot Diameter} = \frac{1.22\lambda_0}{\text{NA}}.$$

Allowing for a focal length of 4.5 mm (to enable at least the required 1-mm imaging depth range), submicron lateral spot diameter was theoretically achievable. A greater challenge came from the requirement for a 1-mm field of view. Imaging over a large

field of view increased the difficulty of designing diffraction-limited optics for high numerical apertures because of axis aberrations, such as astigmatism and coma, increase with field. A trade-off can be made between field of view and numerical aperture to ease the optical design and still achieve diffraction-limited performance. Our lateral resolution and field-of-view specifications could be achieved with a 0.4-NA endoscope provided that the optics performed close to the diffraction limit.

Axial resolution in an optical coherence system is nominally determined by the characteristics of the light source, rather than the sample arm optics. For a Gaussian source spectrum, the axial resolution is proportional to the square of the center wavelength (λ_0) and inversely proportional to the source bandwidth ($\Delta\lambda$, 80 nm in our case), according to the following equation:

$$L_c = 2 \frac{\ln(2)}{\pi} \frac{\lambda_0^2}{\Delta\lambda}.$$

Superluminescent diode (SLD) sources produce axial resolutions ranging from 5 to 15 μm , while a femtosecond laser can produce submicron axial resolution.^{36,37} Our light source produced a theoretical axial resolution of 3.8 μm in air. Therefore, assuming that dispersion was appropriately compensated, axial resolution requirements were easily met.

To appropriately scan the beam, relay through a long endoscope, and focus into the tissue, the optomechanical design of Fig. 2 was implemented. The optical design details for each element are provided in Table 2. The design consisted of a collimating lens, X-Y scanning galvanometer mirrors, scanning doublets, an afocal Hopkins relay, and a 0.4-NA objective. Specifically, the 0.15-NA single-mode fiber was collimated using a 12-mm focal-length achromatic lens, producing a 3.6-mm-diam colli-

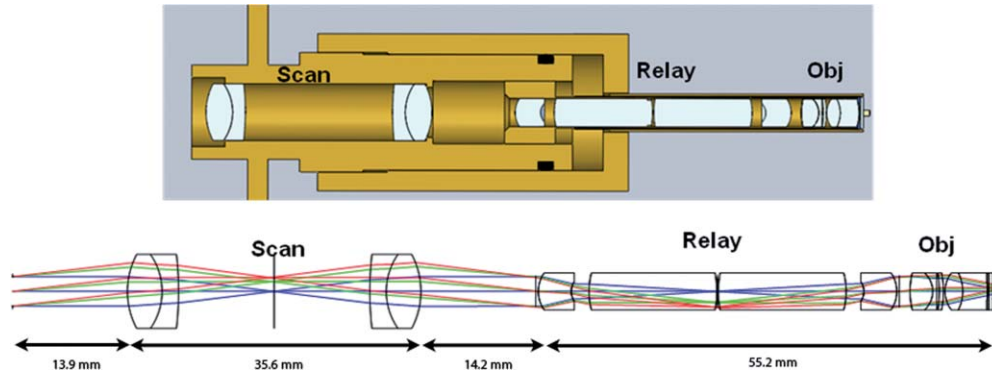


Fig. 2 Optical coherence microscopy endoscope design (Scan = scanning doublets, Relay = Hopkins afocal relay, Obj = objective). Specifications for each of the optics are given in Table 2.

mated beam. The *XY* scanning was performed using a pair of miniature 4-mm *X* and *Y* scanning galvanometer mirrors (Cambridge Technologies, 6210H, Lexington, MA). These scanners enabled image line rates of 600 Hz using a sawtooth waveform with a 70% duty cycle. A pair of scanning doublets relayed the stop between the mirrors to the afocal Hopkins relay stop.

The afocal Hopkins relay³⁸ consisted of two meniscus relay lenses and two high-index glass rod lenses that contain the field lenses. The stop was relayed from the afocal Hopkins relay to the 0.4-NA objective, and the light was focused onto the tissue. The system was modeled in ZEMAX (ZEMAX Development Corporation, Bellevue, Washington), and the simulated best-

Table 2 Endoscope optics specifications.

Component	Part number	Radius of curvature (mm)	Thickness (mm)	Glass type
Collimating lens	EO NT45-784	69.82	1	SFL6
		5.99	3.2	LAKN22
		-6.84		
Scanning doublet (2)	EO NT45-824	9.68	4.2	LAKN22
		-7.91	2	SFL6
		-39.89	23.2	Air
Relay lens (2)	Custom	3.94	4	N-LASF31A
		2.09	2.15	Air
Field lens (2)	Custom	8.8	15.5	N-SF66
		-12	0.2	Air
Objective	Custom	9.8	2.75	N-LAK33A
		-3.06	0.5	N-SF66
		-105.21	0.3	Air
		-16.47	0.5	N-SF66
		-11.29	0.2	Air
		3.74	2.15	N-LAK33A
		-4.93	3	N-SF66
-6.63	0.15 (variable)	Water		
Glass slide	Custom	Infinity	0.5	N-SF66

case system had an Airy disk radius of $1.25\ \mu\text{m}$, corresponding to an ability to visualize a 800-lp/mm feature with 0.1 contrast. The tissue was imaged at the Petzval surface, which had a radius of curvature of 4 mm, causing a full field sag of $31\ \mu\text{m}$.

Once the optical design was complete, a tolerance analysis was performed to determine the effects of errors in the radius of curvature, lens thickness, surface and element tilt, surface and element decentering, surface irregularity, index of refraction, and Abbe number. A sensitivity tolerance analysis and a Monte Carlo tolerance analysis were both performed. A sensitivity tolerance analysis considers the effects on the selected criterion for each tolerance, individually. The aggregate performance is estimated by a root-sum-square calculation, assuming that all the sources of error are acting independently. Initially, all the sources of error were set to have standard precision tolerances to minimize costs, and a sensitivity tolerance analysis was performed to evaluate the “worst offenders,” or sources of error that strongly degrade the image quality. After a list of worst offenders was compiled, the tolerance on each of these offenders was slowly tightened until the image quality was acceptable. The results of this tolerance analysis directed us to design a custom mount to hold the scanning lenses in place that could hold a tight element decentering tolerance. A Monte Carlo simulation is an alternate way of estimating aggregate effects of all tolerances, by generating a series of random lenses that meet the specified tolerances, then evaluating the criterion. The Monte Carlo tolerancing in ZEMAX showed that 0.1 contrast at $720\ \text{lp/mm}$, or an Airy disk radius of $1.4\ \mu\text{m}$, was a realistic expectation.

To allow focusing at various depths in the tissue, the endoscope housing was designed as two pieces screwed together with fine pitch threads. The outer housing contained the distal window, and the inner housing held the refractive optics (Fig. 2). A small rotation of the outer housing moved the lenses proximal and distal relative to the window, causing the focal location in the tissue to change. A complicating factor with most OCM systems is that the path length in the reference arm must be adjusted to account for a change in path length in the sample arm during focusing. The sample arm path length changes because light in the sample arm travels through less air and more tissue as the focus is moved deeper. We avoided this problem in our endoscope design by filling the space between the final objective lens and the window with distilled water. Because the refractive index of tissue is close to water, and the focus was adjusted by $<1\ \text{mm}$, misalignment of the focus and coherence gate in tissue was negligible. The housing was designed to accommodate the displacement of water during focusing. This type of design also enabled optical imaging at a single conjugate, or a single object and image location, which eased the optical design.

The inner and outer endoscope housing was machined out of brass to insure a smooth interface without galling between male and female threads, and to avoid the additional anodization thickness that would have been added if the housing was machined out of aluminum. The 4-mm galvanometer mirrors were mounted and attached to the collimating lens mount and the endoscope housing through the use of three aluminum alignment surfaces. Therefore, when the endoscope was assembled, it was self-aligned. Figure 3 shows the assembled endoscope compared to a penny.

The sample and reference arms on the tabletop OCM system were modified to incorporate the OCM endoscope. The endo-

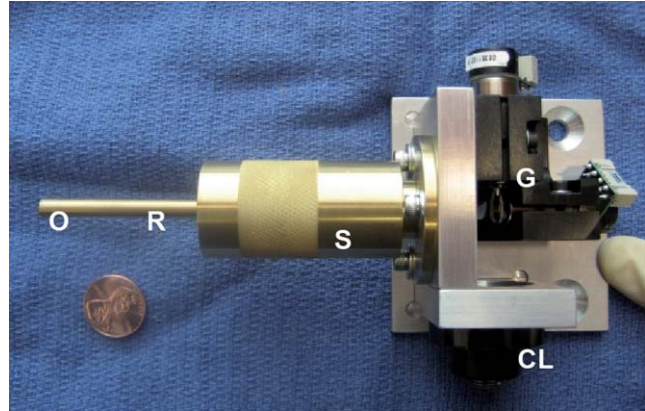


Fig. 3 Assembled OCM endoscope compared to a U.S. penny (CL = collimating lens, G = scanning galvanometer mirrors, S = scanning doublets, R = relay, O = objective).

scope replaced the entire sample arm optomechanics. In the reference arm, a duplicate of the endoscope optics replaced all reference-arm optics, except the piezomounted reference mirror. This replacement was performed to be able to best match dispersion. Because the endoscope contained multiple glass elements with different and sometimes a very high index of refraction, simple compensation with a glass prism pair was insufficient.

The endoscope was characterized by imaging a high-resolution 1951 U.S. Air Force (USAF) negative glass slide resolution target, a mirror, and freshly excised normal mouse ovaries. The ovary images were compared to histology at the corresponding location. Blue tissue marking dye was used to circle the area corresponding to the image location on the mouse ovary. A biopsy at this location was taken and fixed in histochoice tissue fixative (Amersco, Solon, OH) for at least 24 h. The biopsy was then processed, embedded routinely in paraffin, and $6\text{-}\mu\text{m}$ -thick sections were taken. The sectioned tissue was stained with hematoxylin and eosin, photographed, and compared to the OCM images.

3 Results and Discussion

The endoscope met all required physical characteristics. It had a diameter of 6 mm, a length of 34 mm, and an imaging depth range of 1 mm. Optically, the system performed as expected. Figure 4 shows an image of the high-resolution USAF target, imaged in confocal mode (i.e., with the reference arm blocked) to avoid interference fringes. Group 9 element 4, $724\ \text{lp/mm}$ corresponding to a $1.4\text{-}\mu\text{m}$ line-pair feature, is visible with 10% contrast. This corresponds to an Airy disk radius of $1.4\ \mu\text{m}$, which was predicted by the Monte Carlo tolerancing analysis. The axial resolution (full width at half maximum of the signal from a mirror as a function of depth) was measured to be $5.4\ \mu\text{m}$, slightly larger than the theoretical limit. This difference is most likely due to residual dispersion, from manufacturing tolerance differences in the optics of the two endoscopes. The field of view of the endoscope was slightly larger than 1 mm.

The dynamic range of the endoscope-enabled OCM system was measured as the ratio of the signal when it was just saturated to the smallest detectable signal, without adjustment of system parameters, such as gain or reference arm intensity (i.e., the

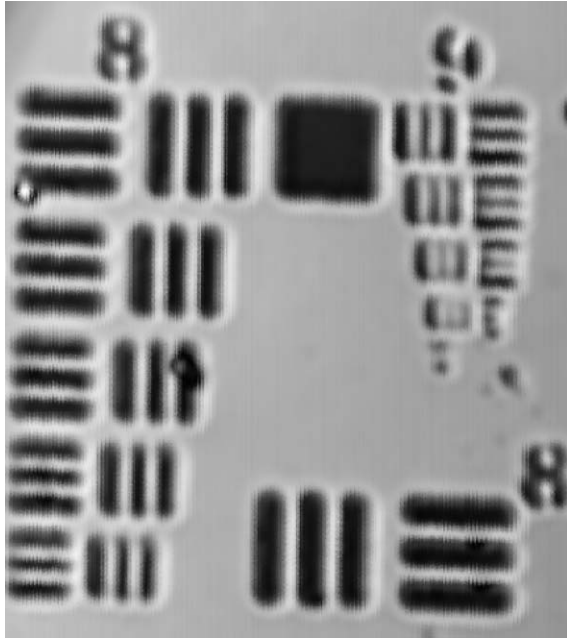


Fig. 4 OCM endoscope confocal image of a 1951 USAF high-resolution target showing group 9, element 4, a $1.4\text{-}\mu\text{m}$ line pair, visible with 0.1 contrast.

variation in signal levels permissible in a single image). Dynamic range was measured by barely saturating the signal then inserting increasing neutral density (ND) filters in the endoscope until the signal-to-noise ratio was 2. Using this technique, the dynamic range was measured to be 76.8 dB. The dynamic range of our system was limited by saturation levels of some analog electronics components. This dynamic range is theoretically sufficient to obtain an image stack in ovary tissue of $>500\ \mu\text{m}$ depth, without requiring system parameter adjustment. Accounting for the ability to modify system settings, ultimate sensitivity was similar to that typically reported for optical coherence systems (e.g., 98 dB for the endoscope enabled OCM system³⁶).

Image acquisition speed was limited by the data acquisition rate (6×10^4 pixels/s) and the endoscope galvanometer scan speed (600 Hz), either of which could be the limiting factor, depending on the size and number of pixels in the image. In practice, the data acquisition rate, not the endoscope design, limited the image frame rate. The 100×100 pixel images across a 1×1 mm full field of view were acquired at a rate of six images per second, whereas a 500×500 pixel image was acquired in 4 s.

Images of freshly excised mouse ovaries and corresponding histology are shown in Figs. 5–7. Figure 5(a) shows an OCM image taken $10\ \mu\text{m}$ below the surface of a left mouse ovary. The two thick arrows point to *corpora lutea*, and the thin arrow points to a possible primary follicle. Figure 5(b) shows an expanded view of the top central *corpus luteum*. Many cell nuclei (small dark ovoid regions) are seen throughout the image and are particularly apparent in the expanded view of Fig. 5(b). Arrowheads point to some of the many nuclei. Figure 5(c) shows a corresponding histology section. Cell nuclei are small dark dots in the histology. Figure 6(a) shows an OCM image taken $10\ \mu\text{m}$ below the surface of another mouse ovary. The long thin arrows point to possible

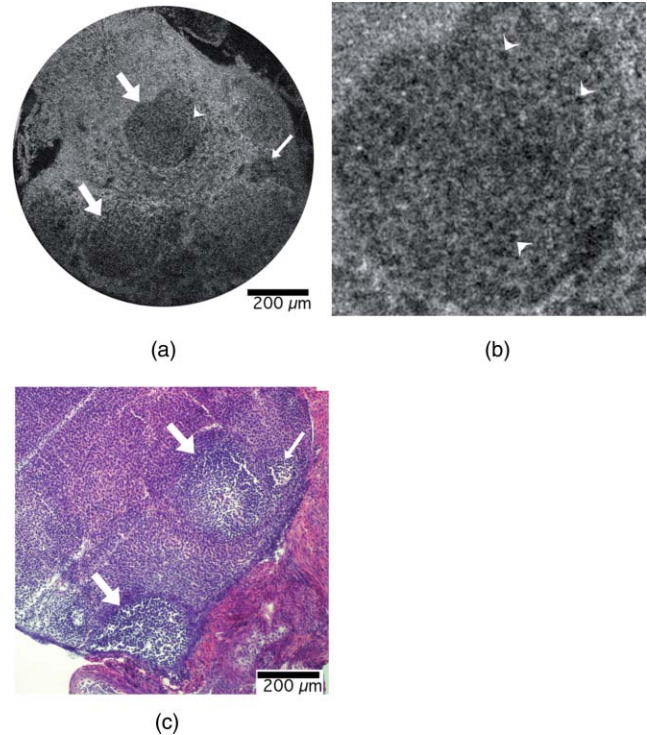


Fig. 5 (a) OCM endoscope image taken $10\ \mu\text{m}$ below the surface of a left mouse ovary. The two thick arrows point to possible *corpus luteum*, and the thin arrow points to a possible primary follicle. Many cell nuclei (small dark ovoid regions, e.g., arrow head) are seen throughout the image. (b) Zoomed-in version of the *corpora lutea* at the top center of the image. Arrow heads point to some of the many cell nuclei. (c) Corresponding histology, arrows defined in (a). Cell nuclei are small dark dots.

large growing or antral follicles. The short thick arrow points to a possible small growing follicle. An expanded view of the two antral follicles is shown in Fig. 6(b). Figure 6(c) shows corresponding histology. Considerable white space is seen in the histology image because the section was taken near the surface of the tissue. One advantage of the OCM endoscope is that the contact method gently compresses ridges in the tissue and creates a smooth flat surface to image. Finally, Fig. 7(a) shows an OCM image taken $50\ \mu\text{m}$ below the surface of a right mouse fallopian tube, which was attached to the ovary on excision. The arrow points to the folds of the tunica mucosa. Figure 7(b) shows an expanded view of the *tunica mucosa* near the arrow. Corresponding histology in Fig. 7(c) shows similar structures.

We found that a 1-mm-diam field of view enabled the ventral surface of a normal mouse ovary to be completely imaged by tiling four to seven images. Therefore, we believe this endoscope design will be appropriate for *in vivo* surgical imaging, allowing high-resolution imaging of the entire mouse ovary surface in a reasonable period of time. In low-pixel-resolution mode (100×100 pixels), the endoscope could be slowly translated across the ovary and images obtained at a frame rate of 6/s. After an area of interest was identified, high-resolution images (500×500 pixels) were obtained. The slow acquisition rate at high resolution provided a challenge for the handheld device. Although operation in contact mode mitigated motion artifacts, future efforts will include a redesign of the analog piezodrives and demodulation electronics to improve pixel acquisition speed.

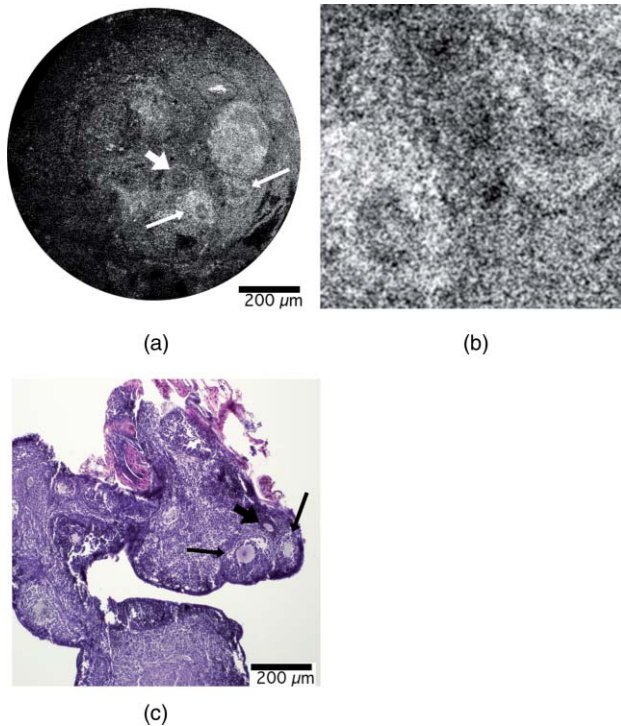


Fig. 6 (a) OCM image taken $10\ \mu\text{m}$ below the surface of a right mouse ovary. The long thin arrows point to possible large growing or antral follicles. The short thick arrow points to a possible small growing follicle. (b) Zoomed-in view of the two antral follicles. (c) Corresponding histology, arrows defined in (a).

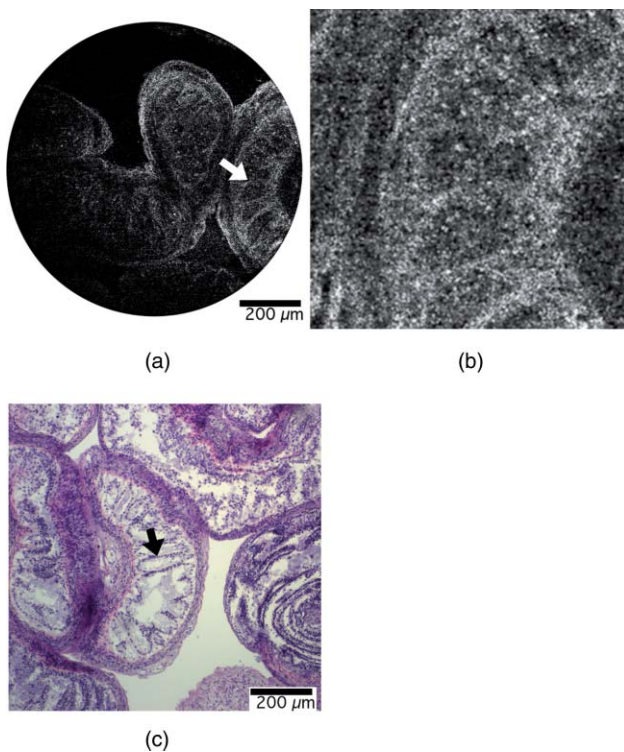


Fig. 7 (a) OCM image taken $50\ \mu\text{m}$ below the surface of a right mouse fallopian tube. The arrow points to the folds of the tunica mucosa. (b) Zoomed-in view around the arrow. (c) Corresponding histology, arrow defined in (a).

In practice, images obtained at large depths ($>300\ \mu\text{m}$) often showed weak signal and somewhat blurry signal features. We believe this image degradation is due to modulations of the tissue index of refraction, leading to a distorted wavefront. Using our endoscope, the focal plane and coherence gate are properly aligned at all depths assuming a tissue bulk index of refraction that is constant and close to water. We were unable to deblur images by changing the reference arm path length, which leads us to believe that our use of water in the endoscope to avoid reference arm adjustments was not the fundamental problem. As light propagates through tissue, the wavefront becomes distorted due to microscale modulations of the tissue index of refraction. Therefore, eventually it becomes impossible to match the coherence gate and focal plane for every point in our relatively large 1-mm-diam field of view, leading to loss of signal and blurring of features. One improvement we could make would be to move to a longer wavelength light source (e.g., $1300\ \text{nm}$). At this wavelength, both tissue scattering and differences in index of refraction of tissue components are lower, which should enable greater depth of imaging with high quality. Obtaining high resolution, however, is a greater challenge at longer wavelengths, as can be seen in the equations for lateral spot diameter and axial resolution. Fortunately, because the small size of the mouse ovary and the ability to image both sides of the organ under light compression, we are able to visualize nearly the complete volume of the ovary with our current design. We can also easily visualize the entire fallopian tube.

4 Conclusion

OCM can provide cellular-level resolution, and an endoscope enables surgical and minimally invasive imaging of internal organs. Our endoscope enables the visualization of structural and cellular features of the mouse ovary, as confirmed by corresponding histology images. This rigid OCM endoscope, which has the smallest diameter and largest field of view reported to date, will primarily be used for minimally invasive surgical imaging in small animals. It may also be convenient to use the handheld endoscope for other applications, such as assessing dysplasia and sun damage in skin during chemoprevention and therapeutic trials.

Acknowledgments

This work was partially supported by NIH Grant No. R01 CA119200.

References

1. D. Huang, E. A. Swanson, C. P. Lin, J. S. Schuman, W. G. Stinson, W. Chang, M. R. Hee, T. Flotte, K. Gregory, C. A. Puliafito, and J. G. Fujimoto, "Optical coherence tomography," *Science* **254**(5035), 1178–1181 (1991).
2. F. Lexer, C. K. Hitzenberger, W. Drexler, S. Molebny, H. Sattmann, M. Sticker, and A. F. Fercher, "Dynamic coherent focus OCT with depth-independent transversal resolution," *J. Mod. Opt.* **46**(3), 541–553 (1999).
3. Y. Liu, Y. Liang, G. Mu, and X. Zhu, "Deconvolution methods for image deblurring in optical coherence tomography," *J. Opt. Soc. Am. A Opt. Image Sci. Vis.* **26**(1), 72–77 (2009).
4. P. D. Woolliams, R. A. Ferguson, C. Hart, A. Grimwood, and P. H. Tomlins, "Spatially deconvolved optical coherence tomography," *Appl. Opt.* **49**(11), 2014–2021 (2010).

5. T. S. Ralston, D. L. Marks, P. S. Carney, and S. A. Boppart, "Inverse scattering for optical coherence tomography," *J. Opt. Soc. Am. A* **23**(5), 1027–1037 (2006).
6. J. P. Rolland, P. Meemon, S. Murali, K. P. Thompson, and K. Lee, "Gabor-based fusion technique for optical coherence microscopy," *Opt. Express* **18**(4), 3632–3642 (2010).
7. S. Murali, P. Meemon, K. S. Lee, W. P. Kuhn, K. P. Thompson, and J. P. Rolland, "Assessment of a liquid lens enabled in vivo optical coherence microscope," *Appl. Opt.* **49**(16), D145–156 (2010).
8. W. Xu, G. T. Bonnema, K. W. Gossage, N. H. Wade, J. Medford, and J. K. Barton, "Customized analog circuit design for fiber-based optical coherence microscopy," *Rev. Sci. Instrum.* **77**, 016104 (2006).
9. B. M. Hoeling, A. D. Fernandez, R. C. Haskell, E. Huang, W. R. Myers, D. C. Petersen, S. E. Ungersma, R. Y. Wang, M. E. Williams, and S. E. Fraser, "An optical coherence microscope for 3-dimensional imaging in developmental biology," *Opt. Express*, **6**(7), 136–146 (2000).
10. O. Nadiarnykh, R. B. LaComb, M. A. Brewer, and P. J. Campagnola, "Alterations of the extracellular matrix in ovarian cancer studied by second harmonic generation imaging microscopy," *BMC Cancer*, **10**(1), 94–107 (2010).
11. G. J. Tearney, S. A. Boppart, B. E. Bouma, M. E. Brezinski, N. J. Weissman, J. F. Southern, and J. G. Fujimoto, "Scanning single-mode fiber optic catheter-endoscope for optical coherence tomography," *Opt. Lett.* **21**(7), 543–545 (1996).
12. G. J. Tearney, M. E. Brezinski, B. E. Bouma, S. A. Boppart, C. Pitris, J. F. Southern, and J. G. Fujimoto, "In vivo endoscopic optical biopsy with optical coherence tomography," *Science* **276**(5321), 2037–2039 (1997).
13. D. C. Adler, Y. Chen, R. Huber, J. Schmitt, J. Connolly, and J. G. Fujimoto, "Three-dimensional endomicroscopy using optical coherence tomography," *Nat. Photon.* **1**(12), 709–716 (2007).
14. W. Jung, D. T. McCormick, Y. Ahn, A. Sepehr, M. Brenner, B. Wong, N. C. Tien, and Z. Chen, "In vivo three-dimensional spectral domain endoscopic optical coherence tomography using a microelectromechanical system mirror," *Opt. Lett.* **32**(22), 3239–3241 (2007).
15. Z. Yaqoob, J. Wu, E. J. McDowell, X. Heng, and C. Yang, "Methods and application areas of endoscopic optical coherence tomography," *J. Biomed. Opt.* **11**(6), 063001 (2006).
16. A. Sergeev, V. Gelikonov, G. Gelikonov, F. Feldchtein, R. Kuranov, N. Gladkova, N. Shakhova, L. Snopova, A. Shakhov, I. Kuznetzova, A. Denisenko, V. Pochinko, Y. Chumakov, and O. Streltsova, "In vivo endoscopic OCT imaging of precancer and cancer states of human mucosa," *Opt. Express*, **1**(13), 432–440 (1997).
17. B. Bouma, *Handbook of optical coherence tomography*, (Marcel Dekker, New York) (2002).
18. E. Zagaynova, N. Gladkova, N. Shakhova, G. Gelikonov, and V. Gelikonov, "Endoscopic OCT with forward-looking probe: clinical studies in urology and gastroenterology," *J. Biophoton.* **1**(2), 114–128 (2008).
19. Y. Wang, M. Bachman, G. Li, S. Guo, B. J. F. Wong, and Z. Chen, "Low-voltage polymer-based scanning cantilever for in vivo optical coherence tomography," *Opt. Lett.* **30**(1), 53–3246 (2005).
20. S. A. Boppart, B. E. Bouma, C. Pitris, G. J. Tearney, J. G. Fujimoto, and M. E. Brezinski, "Forward-imaging instruments for optical coherence tomography," *Opt. Lett.* **22**(21), 1618–1620 (1997).
21. X. Liu, M. J. Cobb, Y. Chen, M. B. Kimmey, and X. Li, "Rapid-scanning forward-imaging miniature endoscope for real-time optical coherence tomography," *Opt. Lett.* **29**(15), 1763–1765 (2004).
22. J. M. Zara, S. Yazdanfar, K. D. Rao, J. A. Izatt, and S. W. Smith, "Electrostatic micromachine scanning mirror for optical coherence tomography," *Opt. Lett.* **28**(8), 628–630 (2003).
23. E. J. Min, J. Na, S. Y. Ryu, and B. H. Lee, "Single-body lensed-fiber scanning probe actuated by magnetic force for optical imaging," *Opt. Lett.* **34**(12), 1897–1899 (2009).
24. L. Huo, J. Xi, Y. Wu, and X. Li, "Forward-viewing resonant fiber-optic scanning endoscope of appropriate scanning speed for 3D OCT imaging," *Opt. Express*, **18**(14), 14375–14384 (2010).
25. S. Moon, S. Lee, M. Rubinstein, B. J. F. Wong, and Z. Chen, "Semi-resonant operation of a fiber-cantilever piezotube scanner for stable optical coherence tomography endoscope imaging," *Opt. Express*, **18**(20), 21183–21197 (2010).
26. J. Wu, M. Conry, C. Gu, F. Wang, Z. Yaqoob, and C. Yang, "Paired-angle-rotation scanning optical coherence tomography forward-imaging probe," *Opt. Lett.* **31**(9), 1265–1267 (2006).
27. S. Han, M. V. Sarunic, J. Wu, M. Humayun, and C. Yang, "Handheld forward-imaging needle endoscope for ophthalmic optical coherence tomography inspection," *J. Biomed. Opt.* **13**(2), 020505 (2008).
28. Y. Pan, H. Xie, and G. K. Fedder, "Endoscopic optical coherence tomography based on a microelectromechanical mirror," *Opt. Lett.* **26**(24), 1966 (2001).
29. T. Xie, H. Xie, G. K. Fedder, and Y. Pan, "Endoscopic optical coherence tomography with a modified microelectromechanical systems mirror for detection of bladder cancers," *Appl. Opt.* **42**(31), 6422–6426 (2003).
30. Z. Wang, C. S. D. Lee, W. C. Waltzer, J. Liu, H. Xie, Z. Yuan, and Y. Pan, "In vivo bladder imaging with microelectromechanical-systems-based endoscopic spectral domain optical coherence tomography," *J. Biomed. Opt.* **12**(3), 034009 (2007).
31. A. Jain, A. Kopa, Y. Pan, G. Fedder, and H. Xie, "A two-axis electrothermal micromirror for endoscopic optical coherence tomography," *IEEE J. Sel. Top. Quantum Electron.* **10**(3), 636–642 (2004).
32. T. Xie, S. Guo, Z. Chen, D. Mukai, and M. Brenner, "GRIN lens rod based probe for endoscopic spectral domain optical coherence tomography with fast dynamic focus tracking," *Opt. Express*, **14**(8), 3238–3246 (2006).
33. T. Xie, G. Liu, K. Kreuter, S. Mahon, H. Colt, D. Mukai, G. M. Peavy, Z. Chen, and M. Brenner, "In vivo three-dimensional imaging of normal tissue and tumors in the rabbit pleural cavity using endoscopic swept source optical coherence tomography with thoracoscopic guidance," *J. Biomed. Opt.* **14**(6), 064045 (2009).
34. A. D. Aguirre, J. Sawinski, S. W. Huang, C. Zhou, W. Denk, and J. G. Fujimoto, "High speed optical coherence microscopy with autofocus adjustment and a miniaturized endoscopic imaging probe," *Opt. Express* **18**(5), 4222–4239 (2010).
35. V. Korde, E. Liebmann, and J. K. Barton, "Design of a handheld optical coherence microscopy endoscope," *Proc. SPIE* **7172**, 71720D (2009).
36. W. Drexler, U. Morgner, F. X. Kartner, C. Pitris, S. A. Boppart, X. D. Li, E. P. Ippen, and J. G. Fujimoto, "In vivo ultrahigh-resolution optical coherence tomography," *Opt. Lett.* **24**(17), 1221–1223 (1999).
37. W. Drexler, "Ultrahigh-resolution optical coherence tomography," *J. Biomed. Opt.* **9**(1), 47–74 (2004).
38. T. H. Tomkinson, J. L. Bentley, M. K. Crawford, C. J. Harkrider, D. T. Moore, and J. L. Rouke, "Rigid endoscopic relay systems: a comparative study," *Appl. Opt.* **35**(34), 6674–6683 (1996).